2024 IEEE/RSJ International Conference on Intelligent Robots and Systems (IROS)
October 14-18, 2024. Abu Dhabi, UAE

# DESectBot: Design and Validation of a Novel Two-Segment Decoupled Continuum Robotic System for Endoscopic Submucosal Dissection

Wenjie Liu[1], Yuancheng Shao[2], Yao Zhang[3], Zixi Chen[4], Di Wu[3], Yuqiao Chen[2], Cesare Stefanini[4], Ling Li[5] and Peng Qi[1]

*Abstract*— **Endoscopic Submucosal Dissection (ESD) is a minimally invasive procedure designed to remove precancerous and cancerous lesions from the gastrointestinal (GI) tract. Given the GI tract's tortuous and narrow shape, along with the need for varied movements during dissection, this requires highly flexible and compact instruments, making flexible continuum robots suitable candidates. In this paper, we propose a novel two-segment continuum robot system named DESectBot, featuring a diameter of 5.5 mm and a total length of the active bending module of 48 mm, while the robot's total length exceeds 1 m. We designed a novel joint combination structure called the spatial cross-curved disk skeleton for the robot, which addresses the mechanical coupling problem between flexible robot actuators. The DESectBot boasts six degrees of freedom, and its kinematic modeling has been derived and utilized in the closed-loop control of the DESectBot. The validation of the DESectBot was conducted through a two-stage test: first, the decoupling performance of the DESectBot was validated. The results show that when one active bending segment bends, the other segment remains almost uninfluenced, with a maximum variation of 1.15 degrees, demonstrating the robot's effective decoupling capability. Secondly, the accuracy of DESectBot was validated through trajectory-following experiments. The results reveal that the average tracking error for both trajectories is less than 2 mm, and the maximum tracking error is below 2.5 mm. Taking marking, one of the ESD procedures with a 5mm tolerance, as an example, the DESectBot has the potential to be utilized for ESD procedure.**

## I. Introduction

Gastric and colorectal cancers currently cause significant mortality rates [1]. Implementing early treatment has become key to improving survival rates [2]. However, the challenges with these cancers often stem from the inner mucosal layer of the gastrointestinal tract, posing difficulties for traditional laparoscopic techniques [3]. To address this issue, clinicians have proposed endoscopic submucosal dissection (ESD) as an effective minimally invasive procedure to treat early stages of gastric and colorectal cancer [4].

Compared to traditional open surgery, ESD using flexible endoscopes offers advantages because it is less invasive, protects organs, and improves patients' quality of life by eliminating the need for incisions [5]. The five key steps of ESD are marking, submucosal injection, mucosal incision, submucosal dissection, and occasional hemostasis [6]. Completing these delicate tasks requires high-level skills, and due to the limited degrees of freedom provided by endoscopes, clinicians need years of training [7]. Additionally, maintaining the stable positioning of the flexible endoscope's tip within the hollow viscera is challenging, especially when targeting mucosal lesions. Improper operation may lead to tissue damage, resulting in serious complications such as perforation and bleeding. Therefore, the instrument should ideally offer multiple resection angles at the target site to effectively reach the lesion.

Continuum robot could serve as a candidate for performing this task. A single port continuum robot platform for transnasal endoscopic minimally invasive surgery was proposed in [8]. Li *et al.* proposed a single segment continuum robotic arm structure for minimally invasive endoscopic surgery [9]. Kim *et al.* introduced a flexible surgical robot platform called (K-FLEX) for the treatment of gastrointestinal regions [10]. Additionally, in [11], [12], a continuum robotic system featuring dual arms was presented for executing ESD.

However, given the intricate nature of ESD, which necessitates precise, small-scale movements while maintaining specific angles, a multi-segment continuum robot may offer greater suitability for such applications. Yang *et al.* developed a dual-arm robotic system for ESD. Its diameter is only 3 mm, which fully satisfies the surgical requirements of ESD [13]. Hwang *et al.* proposed a 17 mm diameter continuum robotic arm called K-FLEX for ESD surgery with enhanced payload capability [14]. In addition, a snake endoscope consisting of an active snake robot and a passive flexible body is proposed. A robot was introduced in [15], which has a seven-degree-of-freedom redundancy that can provide a large internal passage. Furthermore, A micro-rigid joint type continuum robot used for digestive endoscopic minimally invasive surgery was proposed in [16], which has a hyper-redundance driver system and reliable load performance. Xu *et al.* propose a dual-segment continuum robotic arm for single port laparoscopy. The problem with these continuum systems is that it is difficult to decouple multiple segments, but decoupling is a very useful feature in ESD [17], [18]. Therefore, we propose a two-segment and decoupled robot system for ESD surgery.

This paper aims to propose a novel two-segment decoupled

This work is supported by the National Key Research and Development Program of China under Grant No. 2023YFB4705200, and the National Natural Science Foundation of China under Grant No. 62273257. *(Corresponding Author: Peng Qi)*.

[1]Department of Control Science and Engineering, Tongji University, Shanghai 200092, China;

[2]Zhuhai Institute of Advanced Technology, Zhuhai 519085, Guangdong Province, China;

[3] Department of Mechanical Engineering, KU Leuven, Belgium;

[4] the Biorobotics Institute and the Department of Excellence in Robotics and AI, Scuola Superiore Sant'Anna, 56127 Pisa, Italy;

[5] Suzhou Ultimage Health Technology Co., Ltd., Suzhou 215126, Jiangsu Province, China;

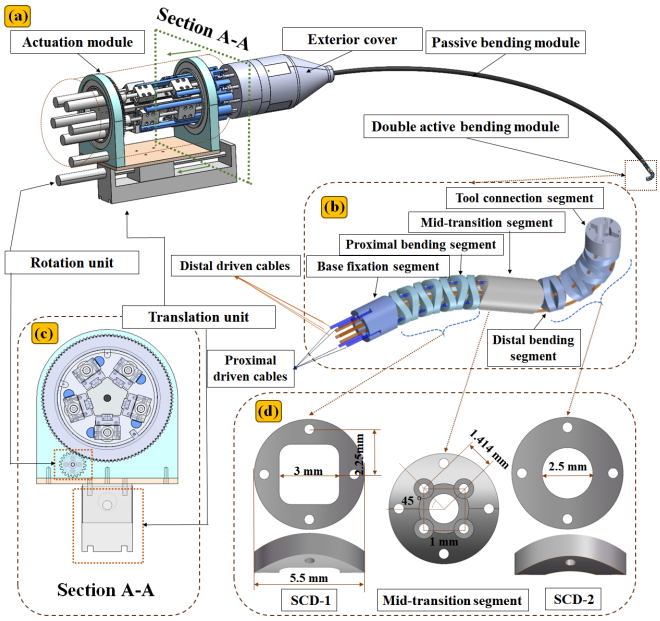


Fig. 1. The overall structure and detailed design of DESectBot: (a) Overall DESectBot structure; (b) a cross-section view on arm driven unit, rotation motion unit, linear motion unit (c) detailed structure of two-segment continuum arm (d) different joint structures in continuum arm.

continuum robotic system called DESectBot for ESD treatment. The main contributions of this paper are summarized as follows:

(1) A novel robotic system named DESectBot is designed, featuring a two-segment structure and decoupling between the two actively bendable segments with six degrees of freedom (DOFs) for ESD treatment. The two-segment continuum arm adopts a novel design using a spatial cross-curved disk skeleton, which can effectively reduce the influence of mechanical coupling.

(2) The inverse kinematics model of DESectBot has been derived to establish the mapping between the robot's actuation space and its joint space.

(3) Experiments are conducted to validate the mechanical decoupling ability and control precision of DESectBot.

The rest of this paper is organized as follows: Section II displays the overall design of the DESectBot, featuring a decoupled operation between two bendable segments. Section III describes the kinematic modeling of the flexible manipulator and analyzes the mapping between actuation space and configuration space. Section IV presents the design of the experiment for validating the decoupling ability and precision of the DESectBot, with the results presented. Finally, Section V concludes this paper.

## II. DESIGN OF THE ROBOTIC SYSTEM

### A. Overall Mechanical System Description

The overall structure of the DESectBot is shown in Fig. 1. The overall robot system is composed of an actuation module, an exterior cover, a passive bending module and a double active bending module, with 6 DOFs to satisfy the requirements of ESD. The DESectBot basic frame is made of light stainless steel. The control system contains seven DC motors (ECXSP16L, Maxon Motor AG, Switzerland) with the specification gearbox GPX16HP (44:1) and is controlled through a multi-axis motion controller (P-MASON0N, Elmo Motion Control Ltd, Israel). The exterior cover is 3D printed and can be easily disassembled. Passive bending module is made of ebonite, with a length of 1 m and its length can be customized according to the actual use. The sheath structures that drive the double active bending module pass through the passive bending module.

As shown in Fig. 1(a) and Fig. 1(c), actuation module has five sets of motors and couplings. Cable fixing sliders are set uniformly along the central axis in a regular pentagon. Four sets of them are used to drive the double active bending module, and the remaining set is employed to control the driven cable of the surgery tool. The nickel-titanium (NiTi) tendons with a diameter of 0.5 mm are used to actuate the active bending module, and the distances from cable fixing sliders to the arm central axis are the same. This configuration ensures the manipulator arm has four DOFs and can achieve various motions with two segments. Furthermore, the rotation motion module and linear motion module can drive the manipulator arm to rotate around its axis and move forward and backward. Overall, with the cooperation of all the above-driven units, the DESectBot has 6 DOFs and can achieve end position and orientation simultaneously.

### B. Dual Continuum Manipulator Mechanism

As shown in Fig. 1(b), the DESectBot has a two-segment active bending module consisting of five main parts: base fixation segment, proximal bending segment, mid-transition segment, distal bending segment and tool connection segment. Considering the narrow cavity space of ESD and effectiveness of torque transmission, the diameter of the DESectBot is 5.5 mm and the overall length is 48 mm. The base fixation segment is a transition connecting the passive bending module to the proximal bending segment. It fixes the internal driven cables of the proximal bending segment in a predetermined arrangement. The mid-transition segment is also a bridge connecting the rear end of the proximal bending segment and the front end of distal bending segment. The tool connection segment is used to install a surgical instrument, such as an electrosurgical generator or surgical clamp.

The driving cables of the distal bending segment will apply extra torque and force to the proximal bending segment [19], which is known as mechanical coupling. It should be noted that the mechanical coupling is the intrinsic property of tendon driven continuum robots, which has a great effect on the stability of multi-section system. Considering the high shear resistance of the NiTi driving tendons, such tendons can also be used as a support structure to form a composite mechanism. Therefore, one driving tendon can be applied as both a transmission component and a part of the skeleton. In this case, there is no integrity constraint requirement on the joint of the continuum, and the joint skeleton design

of the continuum can be simplified. As shown in Fig. 1(b) and Fig. 1(d), both the proximal bending segment and distal bending segment are composed of the spatial cross-curved disk (SCD) joints skeleton. The proximal bending segment is assembled by spatial cross-curved disk-1 (SCD-1), and the other is assembled by spatial cross-curved disk-2 (SCD-2). The proximal bending segment and distal bending segment share the same length (18 mm). A circular curved surface is cut in two vertical directions on the side of the cylindrical SCD disk to form an empty cross-curved disk structure.

As can be seen from Fig. 1(d), the tendon holes are arranged at a uniform 90 degrees interval with a 2.25 mm radius in the proximal bending segment, and the distal tendon holes and proximal ones are staggered by 45 degrees in cross-section. The disk surface is evenly distributed with multiple holes to pass through the corresponding driving tendons. When the two disks are installed as a pair and contact tangentially at the arc surface, the drive tendons pass through the holes in this pair. Then each pair of disks rotates 90 degrees relative to each other. After connection, a cross-arc tangent contact surface is formed on the side of the double active bending module, which can achieve the bending of the double active bending module in four directions.

## III. KINEMATICS MODELING OF THE ROBOTIC SYSTEM

In this section, the kinematics of the robot based on the SCD skeleton is analyzed. Definitions of the coordinate systems and nomenclature of the manipulator are presented in Section III-A. The kinematics of the $i^{th}$ continuum segment and the entire manipulator are described in Section III-B and Section III-C, respectively. Moreover, actuation kinematics with this specific continuum robot are summarized in Section III-D. The Damped Least Square (DLS) method used for motion control of the manipulator is depicted in Section III-E.

### A. Coordinate System Definition

Coordinate systems of the $i^{th}$ continuum segment and the entire manipulator are shown in Fig. 2(a) and (b). The explanation of relevant symbols is shown in Table I.

- World Coordinate System $\{\text{w}\}=\{x_w, y_w, z_w\}$ is located in the base of the robot.
- Base Coordinate System of the $i^{th}$ continuum segment $\{ib\}=\{x_{ib}, y_{ib}, z_{ib}\}$ is attached to the base disk of the $i^{th}$ segment.
- End Coordinate System of the $i^{th}$ continuum segment $\{ne\}=\{x_{ie}, y_{ie}, z_{ie}\}$ is attached to the end disk of the $i^{th}$ segment.
- Bending Plane Coordinate Systems $\{b1\}=\{x_{b1}, y_{b1}, z_{b1}\}$ and $\{\text{b2}\}=\{x_{b2}, y_{b2}, z_{b2}\}$ is attached to the base disk and the end disk of the $i^{th}$ segment with its $x-z$ plane located at the bending plane of the segment.
- Tip Coordinate System $\{tip\}=\{x_{tip}, y_{tip}, z_{tip}\}$ is attached to the tool connection segment.

TABLE I
NOMENCLATURE USED IN KINEMATICS MODELING

| Symbol | Definition |
|---|---|
| $i$ | Index of the continuum segments, i=1,2 |
| $j$ | Index of the driving cables, j=1,2,3,4 |
| $k$ | Index of joints in a single continuum segment, k=1,2,3,4 |
| $n$ | Number of the continuum segments. |
| $m$ | Number of joints in a single continuum segment. |
| $L_0$ | Maximum feeding length of the base rigid segment. |
| $L_i$ | Length of the central backbone of the $i^{th}$ continuum segment. |
| $\theta_i$ | Bending angle of the $i^{th}$ continuum segment. |
| $\delta_i$ | Bending direction angle of the $i^{th}$ continuum segment. |
| $\phi$ | Axial rotation angle of end of the base rigid segment. |
| $d$ | Feeding length of the base rigid segment. |
| $r$ | Distance from the driving cables to the center backbone. |
| $T_b^a$ | Homogeneous transformation matrix from frame $\{b\}$ to frame $\{a\}$. |
| $R_b^a$ | Coordinate rotation matrix from frame $\{b\}$ to frame $\{a\}$. |
| $P_b^a$ | Position vector of frame $\{b\}$ expressed in frame $\{a\}$ |

### B. Kinematics of the $i^{th}$ Continuum Segment

Constant curvature bending assumption is applied to the modeling of continuum manipulator. The configuration space of one continuum segment can be described by $\Psi_i = [\theta_i, \delta_i]^T$. $\theta_i$ and $\delta_i$ denote the bending angle and the bending plane angle, respectively. Therefore, the kinematics of the $i^{th}$ Continuum Segment is obtained as follows.

The homogeneous transformation matrix $T_{ie}^{ib}$ that from the Coordinate System $\{ib\}$ to the Coordinate System $\{ie\}$ is given below.

$$T_{ie}^{ib} = T_{b1}^{ib}\, T_{b2}^{b1}\, T_{ie}^{b2} = \begin{bmatrix} R_{ie}^{ib} & P_{ie}^{ib} \\ O_{1\times 3} & 1 \end{bmatrix} \tag{1}$$

where $P_{ie}^{ib}$ and $R_{ie}^{ib}$ denote the orientation and position of the end disk with respect to the segment base disk.

Therefore, $P_{ie}^{ib}$ and $R_{ie}^{ib}$ are given by

$$P_{ie}^{ib} = \begin{bmatrix} \frac{L_i \cos\delta_i (1-\cos\theta_i)}{\theta_i} \\ \frac{L_i \sin\delta_i (\cos\theta_i - 1)}{\theta_i} \\ \frac{L_i \sin\theta_i}{\theta_i} \end{bmatrix} \tag{2}$$

$$R_{ie}^{ib} = R_{b1}^{ib}\, R_{ni}^{b1}\, R_{ie}^{b1} = \begin{bmatrix} n_x & o_x & a_x \\ n_y & o_y & a_y \\ n_z & o_z & a_z \end{bmatrix} \tag{3}$$

where $n_x = s^2\delta_i + c^2\delta_i c\theta_i$; $n_y = c\delta_i s\delta_i - c\delta_n c\theta_i s\delta_i$; $n_z = -c\delta_i s\theta_i$; $o_x = c\delta_i s\delta_i - c\delta_n c\theta_i s\delta_i$; $o_y = c^2\delta_i + c\theta_i s^2\delta_i$; $o_z = -s\theta_i s\delta_i$; $a_x = c\delta_i s\theta_i$; $a_y = s\delta_i s\theta_i$; $a_z = c\theta_i i$.

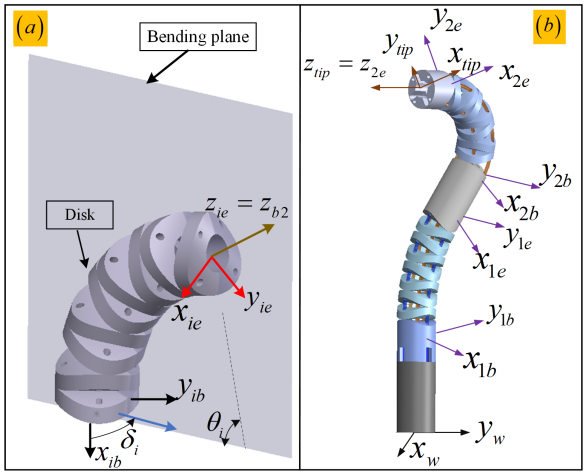


Fig. 2. Coordinate systems and modeling of the active bending module: (a) the representation of the $i^{th}$ active bending segment; (b) the entire active bending module.

In the above formulas, $s$ and $c$ denote the trigonometric function $sin$ and $cos$ respectively.

The instantaneous inverse kinematics of the $i^{th}$ continuum segment is given by:

$$\dot{x_i} = J_{\Psi_i}\dot{\Psi}_i \tag{4}$$

where $\dot{\Psi}_i = [\dot{\theta}_i, \dot{\delta}_i]^T$ is a velocity vector of configuration space for the segment, $\dot{x_i} = [\dot{v}_i, \dot{w}_i]^T$ is a velocity vector of the center of the end disk, and $J_{\Psi_i}$ is a jacobian matrix.

Then, elements in each row and column $J_{\Psi_i}$ are described in the following equation.

$$J_{\Psi_i} = \begin{bmatrix} \frac{L_i s\delta_i (c\theta_i - 1)}{\theta_i} & \frac{L_i c\delta_i (c\theta_i - 1)}{\theta_i^2} + \frac{L_i c\delta_i s\theta_i}{\theta_i} \\ -\frac{L_i c\delta_i (c\theta_i - 1)}{\theta_i} & \frac{L_i s\delta_i s\theta_i}{\theta_i} + \frac{L_i s\delta_i (c\theta_i - 1)}{\theta_i^2} \\ 0 & \frac{L_i c\theta_i}{\theta_i} - \frac{L_i s\theta_i}{\theta_i^2} \\ -s\delta_i s\theta_i & c\delta_i \\ -c\delta_i s\theta_i & -s\delta_i \\ 1 - c\theta_i & 0 \end{bmatrix} \tag{5}$$

### C. Kinematics of the Entire Continuum Manipulator

Based on the kinematics of one single continuum segment, the whole kinematics model of the entire continuum robot can be established. The coordinate systems for the entire manipulator are shown in Fig. 2(b).

- The rotation and linear motion units in MCRS have 2 DOFs for rotation and feed along the $z_w$-axis. These two types of motion are respectively parameterized by $\phi$ and $d \in [0, L_0]$.
- The continuum segment 1 (proximal bending segment) is connected to the end of the base fixation segment. The state of its motion is represented by $\theta_1$ and $\delta_1$.
- The continuum segment 2 (distal bending segment) is located between the segment 1 and the tool connection segment. The state of its motion is parameterized by $\theta_2$ and $\delta_2$.

The kinematics of the entire manipulator can be parameterized by configuration space $\Psi = [d, \phi, \theta_1, \delta_1, \theta_2, \delta_2]^T$. The representation matrix of the tip coordinate system {tip} relative to the world coordinate system {w} is given by:

$$T_{tip}^{w} = T_{1b}^{w} T_{1e}^{1b} T_{2b}^{1e} T_{2e}^{2b} T_{tip}^{2e}. \tag{6}$$

The instantaneous inverse kinematics of the entire manipulator is given by:

$$\dot{x} = J_{\Psi}\dot{\Psi} \tag{7}$$

where $J_{\Psi}$ is jacobian matrix of the entire continuum manipulator derived from $J_{\Psi_i}$, $d$, and $\phi$. $\dot{x}$ is the velocity of the tip.

### D. Inverse Kinematics

Given a tip target position $P_d$, the difference $dP_e$ between it and the actual position $P_a$ can be obtained as in Eq. (8). Following [20], we estimate the derivative terms by a first-order approximation, and the differential relationship between the tip displacement $dP_e$ and configuration variation $d\Psi$ can also be derived as follows.

$$dP_e = P_d - P_a = J_{\Psi} d\Psi \tag{8}$$

Therefore, supposing $dP_e$ is target displacement, joint variation $d\Psi$ can be obtained as in Eq. (9) to further drive the motor to undergo corresponding changes.

$$d\Psi = J_{\Psi}^{+} dP_e \tag{9}$$

To avoid the pseudo-inverse method's problems with singularity, the damped least square (DLS) is used to improve numerical stability. The specific description of $J_{\Psi}^{+}$ is as follows.

$$J_{\Psi}^{+} = J_{\Psi}^{T}(J_{\Psi} J_{\Psi}^{T} + \lambda I)^{-1} \tag{10}$$

where the damping constant $\lambda = 0.15$ is chosen.

The numerical iteration method is implemented to achieve inverse kinematic control. After updating the configuration vector $\Psi(k+1) = \Psi(k) + d\Psi(k)$ at the $kth$ time, actuation kinematics calculates the commands of cable motion and sends them to the controller. In the next time step, the current tip position is calculated from forward kinematics through the configuration vector and further compared with the new target tip position.

### E. Kinematics of the Actuation

The kinematics from configuration space to actuation space varies with the structure of the continuum manipulator. Under the assumption that the bending angles of each disk in the same continuum segment are equal, this section describes the mapping from configuration space to actuation space.

As shown in Fig. 3, since the lengths of the tendons inside the disk are constant, only the lengths of the tendons in the gap between the disks should be considered in the actuation kinematics model. The driving tendons between adjacent disks are straight, which can be written as:

$${}^{k}l_{ij}^{gap}(\beta_{ij}) = 2rc\left(\delta_i + \frac{\pi(j-1)}{2}\right) s\left(\beta_0 + \frac{\beta_{ij}}{2}\right) \tag{11}$$

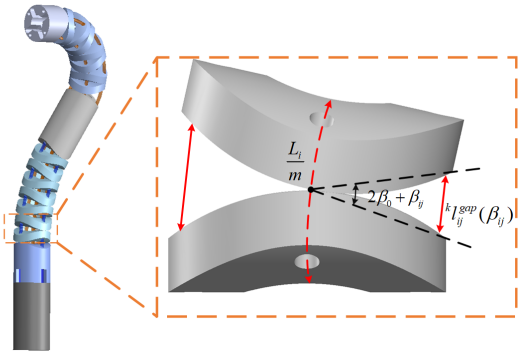


Fig. 3. Bending model between adjacent disks.

where $\beta_{ij} = \frac{\theta_i}{m}$, which is the angle variations of adjacent disks gap, ranging from $-16°$ to $16°$, from the initial angle of gap $\beta_0$. Moreover, $s$ and $c$ denote $sin$ and $cos$ respectively.

The cable length variations are shown as Eq. (12) when the manipulator moves from the initial to the desired state.

$$\Delta l_{ij}^k = {}^k l_{ij}^{gap}(\beta_{ij}) - {}^k l_{ij}^{gap}(0) \tag{12}$$

Therefore, cable length variations in one segment composed of four joint groups can be given in below:

$$\Delta L_{ij}^n = 4\Delta l_{ij}^k \tag{13}$$

Furthermore, the displacement of driving cable for the $i^{th}$ continuum segment can be expressed as:

$$\Delta L_{ij} = \sum_{i=1}^{n} \Delta L_{ij}^n \tag{14}$$

In addition, due to the driving tendons of the distal bending segment passing through the proximal bending segment, the proximal segment will have an impact on the bending of the distal bending segment. Therefore, when calculating the total length of each driving cable, the distal segment cable length needs to be compensated according to Eq. (14).

## IV. Experimental Validation

The following experiments will be carried out to investigate and verify the performance of DESectBot.

### A. Experimental Setup

As illustrated in Fig. 1, the DESectBot is comprehensively introduced in Section II-A. It features a passive bending module exceeding 1 m in length, designed for endoscopic applications. To more effectively concentrate on and characterize its essential component, namely the double active bending module, we have purposely built an experimental setup. This setup includes the actuation module and the double active bending module, but with a shortened length of the passive bending module, as depicted in Fig. 4. The electromagnetic tracking system (Northern Digital Inc., Canada) is employed to track the actual tip position of the robot. This system is connected to a host PC (Intel Core i5-10400F-2.90GHz) via a Local Area Network (LAN). A single eletromagnetic

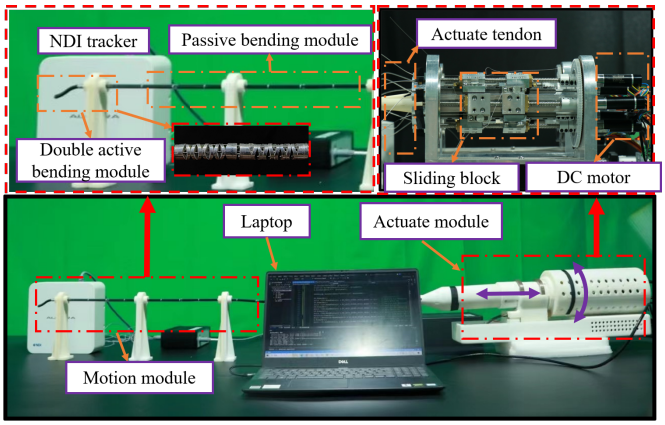


Fig. 4. Experimental setup for trajectory tracking and mechanical decoupling.

(EM) sensor (Northern Digital Inc., Canada) with 6 DOFs is affixed to the central hole of the active bending module, with its local coordinate system pre-defined. The EM sensor measures position and orientation with respect to the local coordinate system at a rate of 25 Hz. To ensure real-time posture information of the robot in each servo loop, the servo cycle is set to be longer than the EM's sampling time, specifically chosen to be 40 ms.

### B. Validation of the Robot's Decoupling Capability

Constructed upon the SCD skeleton, the two-segment continuum arm can independently bend its distal and proximal segments. This indicates that each bending segment can achieve the desired angle while the other segment remains unaffected.

To validate the decoupling bending performance of the two active bending segments, two experiments were conducted. In the first experiment, the distal segment remained stationary, while the proximal bending segment was manipulated from a straight configuration to a $60°$ angle. To document the angle variation of the proximal segment during the experiment, a camera was utilized to capture the robot bending at 10-degree intervals, as presented in Fig. 5(a). In the second experiment, the proximal segment remained straight, while the distal bending segment was bent from a straight configuration to $60°$. As depicted in Fig. 5(b), the movement of the distal bending segment was captured at every $10°$ interval. The coupling error, representing the influence of the actuated segment on the unactuated segment's bending angle, provides insights into the mutual coupling of the adjacent continuum segments. It is important to note that, in the first experiment set, due to mechanical connection, the corresponding movement of the distal segment induced by the proximal bending is inevitable. Therefore, the coupling error for the first experiment set signifies the distal segment's bending radius in comparison to the straight status.

As indicated in TABLE II, the average coupling error for the proximal and distal decoupling experiments is $0.98°$ and $1.04°$, respectively. This highlights a good decoupling performance between the proximal and distal segments.

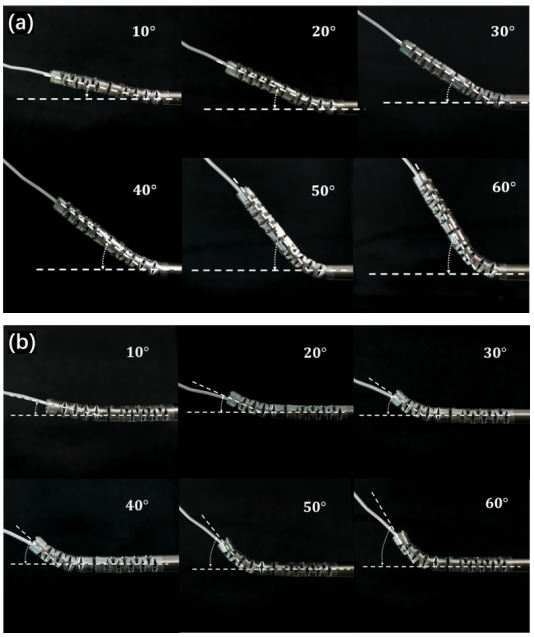


Fig. 5. Experimental results of mechanical decoupling of (a) the proximal segment and (b) the distal segment.

TABLE II
MECHANICAL DECOUPLING EXPERIMENT RESULTS

| Bending Angle (°) | 10 | 20 | 30 | 40 | 50 | 60 |
|---|---|---|---|---|---|---|
| Coupling error (Case1) (°) | 0.76 | 0.87 | 1.05 | 1.15 | 0.98 | 1.09 |
| Coupling error (Case2) (°) | 0.81 | 0.90 | 0.63 | 1.05 | 1.15 | 1.07 |

Case 1: The proximal segment bends while the distal segment remains unactuated.
Case 2: The distal segment bends while the proximal segment remains unactuated.

### C. Trajectory Tracking

In the context of ESD, intricate trajectories involving both straight and curved lines are essential for the completion of the treatment. To verify the accuracy of the DESectBot and its kinematic modeling, trajectory tracking experiments were conducted. In this study, square and semicircular trajectories in the $x-y$ plane, as illustrated in Fig. 2, were selected to demonstrate the robot's capability to navigate both straight and curved paths. The performance of DESectBot in trajectory following is evaluated based on the average Euclidean distance between the actual and the desired trajectories, as defined by the equation below:

$$error = \sqrt{(x_r - x)^2 + (y_r - y)^2} \tag{15}$$

where $x_r$ is x coordinate of the reference trajectory, $y_r$ is y coordinates of the reference trajectory. $x$ and $y$ are coordinates of the experimental trajectory.

In the first experiment, the robot was controlled to follow a square trajectory, each side measuring 30 mm in length. As illustrated in Fig. 6(a), the bending segment successfully traces the trajectory, starting from the green point (0, 0) and concluding at the red point (15, 0). The actual trajectory, recorded by the EM sensors, is represented by the blue line and compared with the desired trajectory in green. To further illustrate the trajectory tracking performance of the two-segment bending component, the performance in the $x$ and $y$ axis is presented in Fig. 6(b) and Fig. 6(c), respectively. The tracking error, computed according to Eq. (15), is depicted in Fig. 6(d), revealing an average tracking error of 1.9 mm and a maximum tracking error of 2.4 mm.

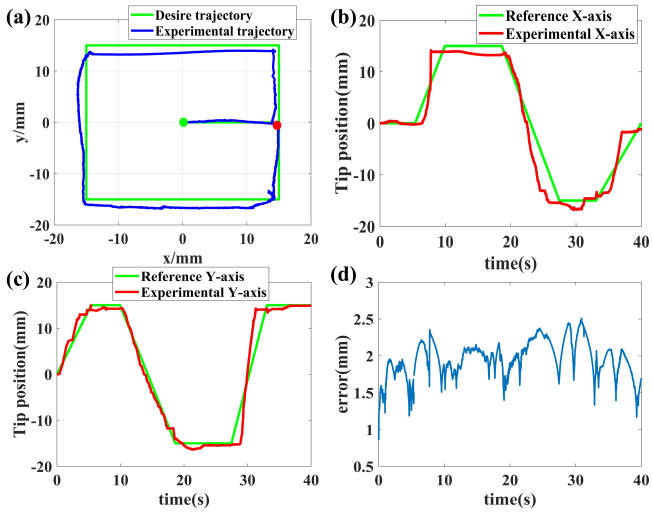


Fig. 6. Experimental results of rectangular trajectory tracking: (a) rectangular case. Curves of x and y coordinates with respect to time in (b) and (c). rectangular trajectory tracking error (d)

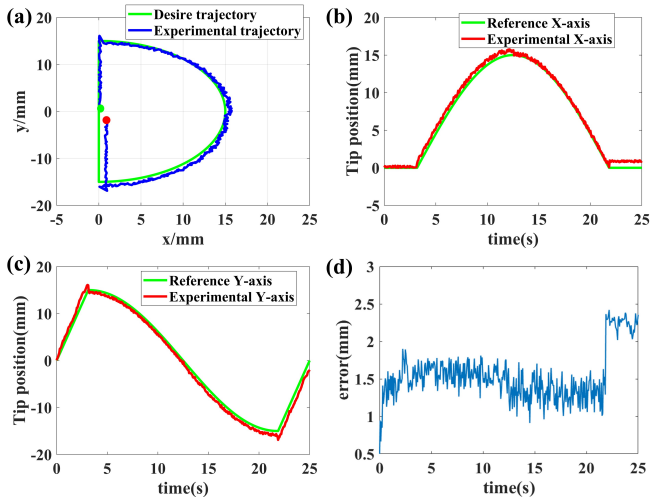


Fig. 7. Experimental results of semicircular trajectory tracking. (a) Semicircular case. Curves of x and y coordinates with respect to time in (b) and (c). semicircular trajectory tracking error (d)

In the second experiment, a semicircle trajectory with a 15 mm radius was employed to assess the performance of the proposed two-segment bending component. As depicted in Fig. 7(a), the starting and ending points of the desired trajectory (green) are both at the origin point (0, 0). The actual tracking trajectory closely follows the desired trajectory in the circular segment, with an average error of approximately

1.5 mm. However, the error increases to around 2.5 mm due to an offset between the actual and the desired trajectories in the straight part of the semicircle. The performance of the bending segment in the $x$ and $y$ axis is illustrated in Fig. 7(b) and Fig. 7(c), respectively. The tracking error, also based on the calculation of Eq. (15), is presented in Fig. 7(d). The results indicate an average tracking error and a maximum tracking error of $1.5$ mm and $2.1$ mm, respectively.

The results of the two experiments underscore the promising performance of DESectBot. The average tracking error for both trajectories remains below 2 mm, while the maximum tracking error does not exceed 2.5 mm. Considering the initial marking step of ESD, which is a crucial procedure that involves outlining the boundaries around a lesion or area of interest in the GI tract and requires a tolerance of 5 mm, the proposed DESectBot successfully meets this requirement in terms of accuracy [21].

## V. Conclusion and Future Work

This paper presents the DESectBot, a continuum robotic system equipped with two decoupled bending segments. These segments enhance the robot's flexibility, maneuverability, and environmental adaptability. The control of the active bending modules is facilitated through a kinematic model that examines the relationship between the actuators and the end effector, establishing a connection between the displacement of the driving cables and the configuration space. Experiments were conducted to validate the system's decoupling capabilities and precision. The results highlight the DESectBot's ability to independently operate the two active bending segments and accurately follow 2D trajectories, satisfying the precision demands of ESD treatments.

For simplicity, the system functionality was validated with a shortened passive bending segment. However, extending the length of the passive bending segments for realistic ESD surgeries will inevitably increase the friction between the wires and the robot's materials, thereby amplifying the system's nonlinear phenomena such as hysteresis. Future work will focus on modeling and compensating for hysteresis to mitigate its impact during operation [22]. Moreover, given the complexity of the robotic system, deep learning methods specifically for multi-segment robots will be explored for controlling the DESectBot in future studies.

## References


[1] A. Jemal, F. Bray, M. M. Center, J. Ferlay, E. Ward, and D. Forman, "Global cancer statistics," *CA: a cancer journal for clinicians*, vol. 61, no. 2, pp. 69–90, 2011.

[2] S. Oka, S. Tanaka, I. Kaneko, R. Mouri, M. Hirata, T. Kawamura, M. Yoshihara, and K. Chayama, "Advantage of endoscopic submucosal dissection compared with emr for early gastric cancer," *Gastrointestinal endoscopy*, vol. 64, no. 6, pp. 877–883, 2006.

[3] R. Nakadate, T. Iwasa, S. Onogi, J. Arata, S. Oguri, Y. Okamoto, T. Akahoshi, M. Eto, and M. Hashizume, "Surgical robot for intraluminal access: An ex vivo feasibility study," *Cyborg and Bionic Systems*, 2020.

[4] J. T. Maple, B. K. A. Dayyeh, S. S. Chauhan, J. H. Hwang, S. Komanduri, M. Manfredi, V. Konda, F. M. Murad, U. D. Siddiqui, and S. Banerjee, "Endoscopic submucosal dissection," *Gastrointestinal endoscopy*, vol. 81, no. 6, pp. 1311–1325, 2015.

[5] T. Oyama, A. Tomori, K. Hotta, S. Morita, K. Kominato, M. Tanaka, and Y. Miyata, "Endoscopic submucosal dissection of early esophageal cancer,"*Clinical Gastroenterology and Hepatology*, vol. 3, no. 7, pp. S67–S70, 2005.

[6] S. V. Kantsevoy, D. G. Adler, J. D. Conway, D. L. Diehl, F. A. Farraye, R. Kwon, P. Mamula, S. Rodriguez, R. J. Shah, L. M. W. K. Song et al., "Endoscopic mucosal resection and endoscopic submucosal dissection," *Gastrointestinal endoscopy*, vol. 68, no. 1, pp. 11–18, 2008.

[7] A. Y. B. Teoh, P. W. Y. Chiu, S. K. H. Wong, J. J. Y. Sung, J. Y. W. Lau, and E. K. W. Ng, "Difficulties and outcomes in starting endoscopic submucosal dissection," *Surgical endoscopy*, vol. 24, pp. 1049–1054, 2010.

[8] J. Shang, K .Leibrandt, P. Giataganas, V. Vitiello, C. A. Seneci, P. Wisanuvej, J. Liu, G. Gras, J. Clark, A. Darzi, G.Yang . "A single-port robotic system for transanal microsurgery—Design and validation." *IEEE robotics and automation letters*. vol.2, no, 3, pp 1510-1517, 2017.

[9] C. Li, X. Gu, X. Xiao, C. M. Lim, H. Ren, "A robotic system with multichannel flexible parallel manipulators for single port access surgery". *IEEE transactions on industrial informatics*, vol.15, no, 3, pp 1678-1687, Mar, 2019.

[10] J. Kim, M. Hwang, D. Lee, H. Kim, J. Ahn, J. You, D. h. Baek, D. S. Kwon. "Effects of flexible surgery robot on endoscopic procedure: Preliminary bench-top user test." *2019 28th IEEE International Conference on Robot and Human Interactive Communication (RO-MAN)*. IEEE, 2019 , pp 1-6.

[11] K. C. Lau, Y . Hu, Y . Y . Leung, C. C. Y . Poon, P . W. Y . Chiu, J. Y . W. Lau, Y . Yam. "Design and development of a task specific robot for endoscopic submucosal dissection of early gastrointestinal cancers." *2014 International Symposium on Optomechatronic Technologies*. IEEE, 2014.

[12] K. C. Lau, E. Y. Y. Leung, P. W. Y. Chiu, Y. Yam, J. Y. W. Lau, C. C. Y. Poon. "A flexible surgical robotic system for removal of early-stage gastrointestinal cancers by endoscopic submucosal dissection". *IEEE Transactions on Industrial Informatics*, vol. 12, no. 3, pp 2365-2374, Dec, 2016.

[13] X. Yang, H. Gao, S. Fu, R. Ji, C.Hou, H.Liu, N. Luan, H. Ren, L.Sun, J. Yang, X.Zuo. "Novel miniature transendoscopic telerobotic system for endoscopic submucosal dissection (with videos)." *Gastrointestinal Endoscopy*, vol. 99, no. 2, pp 155-165, 2024.

[14] M. Hwang, D. S. Kwon. "K-FLEX: a flexible robotic platform for scar-free endoscopic surgery." *The International Journal of Medical Robotics and Computer Assisted Surgery*, vol. 16, no.2, pp e2078, Jan, 2020.

[15] W. Li, M. Shen, A. Gao, G. Z. Yang, B. Lo. "Towards a snake-like flexible robot for endoscopic submucosal dissection". *IEEE Transactions on Medical Robotics and Bionics*, vol. 3, no. 1, pp 257-260, Feb, 2021.

[16] C. Li, Y. Yan, X. Xiao, X. Gu, H. Gao, X. Duan, X. Zuo, Y. Li, and H. Ren, "A miniature manipulator with variable stiffness towards minimally invasive transluminal endoscopic surgery," *IEEE robotics and automation letters*, vol. 6, no. 3, pp. 5541-5548, Jul, 2021.

[17] K. Xu, J. Zhao, and M. Fu, "Development of the sjtu unfoldable robotic system (surs) for single port laparoscopy," *IEEE/ASME Transactions on Mechatronics*, vol. 20, no. 5, pp. 2133–2145, 2014.

[18] Z. Wu, Q. Li, J. Zhao, J. Gao, and K. Xu, "Design of a modular continuumarticulated laparoscopic robotic tool with decoupled kinematics," *IEEE robotics and automation letters*, vol. 4, no. 4, pp. 3545–3552, Oct. 2019.

[19] W. Ba, X. Dong, A. Mohammad, M. Wang, D. Axinte, and A. Norton, "Design and validation of a novel fuzzy-logic-based static feedback controller for tendon-driven continuum robots," *IEEE/ASME Transactions on Mechatronics*, vol. 26, no .6, Dec, 2021.

[20] M. C . Yip, D. B. Camarillo. "Model-less feedback control of continuum manipulators in constrained environments." *IEEE Transactions on Robotics*, vol. 30, no. 4, pp. 880-889, 2014.

[21] B. Cetinsaya, M. A. Gromski, S. Lee, Z. Xia, D. Demirel, T. Halic, C. Bayrak, C. Jackson, S. De, S. Hegde et al., "A task and performance analysis of endoscopic submucosal dissection (esd) surgery," *Surgical endoscopy*, vol. 33, pp. 592–606, 2019.

[22] D. Wu *et al.*, "Hysteresis modeling of robotic catheters based on long short-term memory network for improved environment reconstruction," *IEEE Robotics and Automation Letters*, vol. 6, no. 2, pp. 2106–2113, 2021